nature physics

Article

https://doi.org/10.1038/s41567-023-02318-7

One-ninth magnetization plateau stabilized by spin entanglement in a kagome antiferromagnet

Received: 11 June 2022

Accepted: 3 November 2023

Published online: 12 January 2024

Check for updates

Sungmin Jeon[1,13], Dirk Wulferding[2,3,13], Youngsu Choi[4], Seungyeol Lee[1], Kiwan Nam[5], Kee Hoon Kim[5], Minseong Lee[6], Tae-Hwan Jang[7], Jae-Hoon Park[7,8], Suheon Lee[9,10], Sungkyun Choi[9,10], Chanhyeon Lee[11], Hiroyuki Nojiri[12] & Kwang-Yong Choi[1]

The spin-1/2 antiferromagnetic Heisenberg model on a kagome lattice is geometrically frustrated, which is expected to promote the formation of many-body quantum entangled states. The most sought-after among these is the quantum spin-liquid phase, but magnetic analogues of liquid, solid and supersolid phases may also occur, producing fractional plateaus in the magnetization. Here, we investigate the experimental realization of these predicted phases in the kagome material $YCu_3(OD)_{6+x}Br_{3-x}$ ($x \approx 0.5$). By combining thermodynamic and Raman spectroscopic techniques, we provide evidence for fractionalized spinon excitations and observe the emergence of a 1/9 magnetization plateau. These observations establish $YCu_3(OD)_{6+x}Br_{3-x}$ as a model material for exploring the 1/9 plateau phase.

One of the most sought-after many-body phenomena in the field of quantum magnets is a quantum spin liquid (QSL), a long-range entangled spin state that negates the standard symmetry-breaking paradigm. QSLs feature fractionalized quasiparticles and emergent gauges[1–4]. In the quest to realize QSLs, an $s = 1/2$ kagome Heisenberg antiferromagnet (KHAF), which is a two-dimensional lattice formed by corner-sharing triangles, is proposed for a paradigmatic setting for emergent QSLs. Accumulating numerical evidence supports the existence of a QSL ground state in a KHAF, yet its precise nature remains unsettled, with two potential flavours: a Z_2 gapped QSL and a gapless U(1) liquid[5–13].

Aside from the probable zero-field QSL, the application of a magnetic field to a KHAF engenders exotic quantum phases at fractional magnetization plateaus $m = 1/9, 3/9, 5/9$ or $7/9$ (refs. 14–28). The kinetic frustration induces the crystallization of magnons localized on the hexagon of the kagome lattice at $m = 3/9, 5/9$ or $7/9$, resulting in spin-gapped solid phases. Additionally, a supersolid phase emerges just below the $m = 5/9$ plateau. On the other hand, the nature of the 1/9 magnetization plateau, which is stabilized by spin entanglement, remains subject to controversy, with the possibility of it being a topological Z_3 spin liquid or valence bond crystals[21,26,28]. Despite the fundamental interest in the 1/9 plateau phase, its experimental realization has proven elusive due to the lack of adequate materials, presenting a long-standing challenge in kagome physics.

To date, a number of $s = 1/2$ kagome compounds, including herbertsmithite $ZnCu_3(OH)_6Cl_2$, kapellasite α-$Cu_3Zn(OH)_6Cl_2$ and Zn-barlowite $Cu_3Zn(OH)_6FBr$ (refs. 29–36), have been reported as

[1]Department of Physics, Sungkyunkwan University, Suwon, Republic of Korea. [2]Center for Correlated Electron Systems, Institute for Basic Science, Seoul, Republic of Korea. [3]Department of Physics and Astronomy, Seoul National University, Seoul, Republic of Korea. [4]Department of Energy Science, Sungkyunkwan University, Suwon, Republic of Korea. [5]Center for Novel States of Complex Materials Research, Department of Physics and Astronomy, Seoul National University, Seoul, Republic of Korea. [6]National High Magnetic Field Laboratory (NHMFL), Los Alamos National Laboratory (LANL), Los Alamos, NM, USA. [7]MPPHC-CPM, Max Planck POSTECH/Korea Research Initiative, Pohang, Republic of Korea. [8]Department of Physics, Pohang University of Science and Technology, Pohang, Republic of Korea. [9]Center for Integrated Nanostructure Physics, Institute for Basic Science, Suwon, Republic of Korea. [10]Sungkyunkwan University, Suwon, Republic of Korea. [11]Department of Physics, Chung-Ang University, Seoul, Republic of Korea. [12]Institute for Materials Research, Tohoku University, Sendai, Japan. [13]These authors contributed equally: Sungmin Jeon, Dirk Wulferding. e-mail: choisky99@skku.edu

https://doi.org/10.1038/s41567-023-02318-7

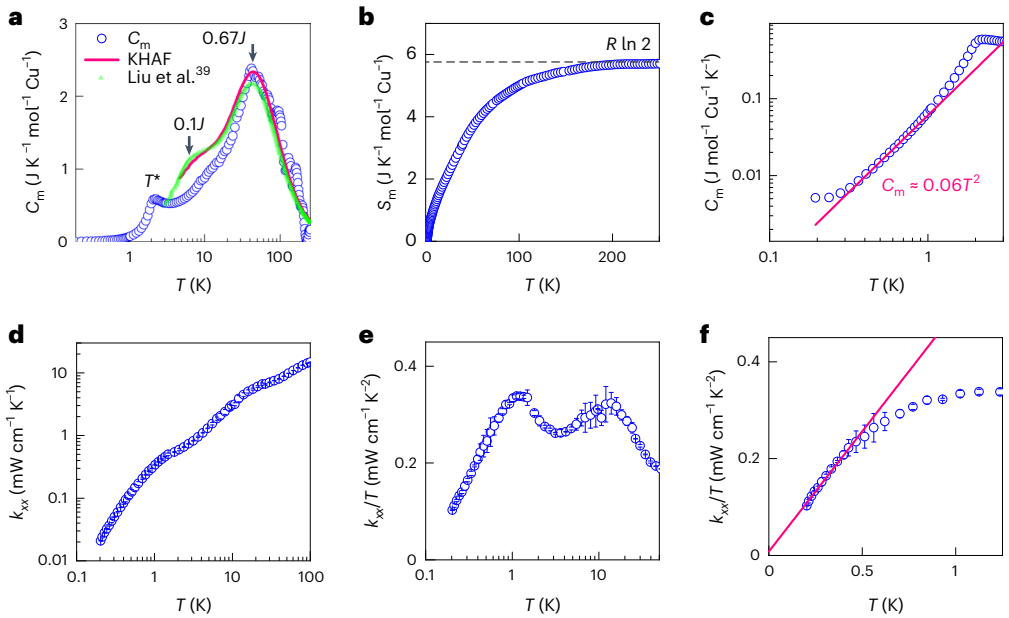

Fig. 1 | Magnetic specific heat and thermal conductivity of $YCu_3(OD)_{6.5}Br_{2.5}$. **a**, Semi-log plot of the magnetic specific heat (C_m; open circles) versus temperature T obtained after subtracting the lattice contribution. The pink line and green triangles represent numerical calculations of C_m for an ideal kagome antiferromagnet[39]. The two vertical arrows denote two characteristic temperatures at $0.1J$ and $0.67J$, and T^* represents a weak specific anomaly. **b**, Magnetic entropy S_m versus T calculated by integrating $C_m(T)/T$. In the high-temperature limit, the full R ln 2 spin entropy (horizontal dashed line) is recovered. **c**, The very low-temperature C_m in a log–log scale. The solid line indicates a power-law behaviour $C_m \propto T^2$. **d**, Plot of thermal conductivity κ versus T to a log–log scale. **e**, Semi-log plot of κ/T versus T. **f**, Temperature dependence of κ/T in the range $T = 0.2$–1.25 K. The solid red line represents a linear fit of κ/T. The thermal conductivity was measured three times at each temperature and the data points were subsequently averaged. The error bars in **d**–**f** indicate the standard deviation of the data points.

QSL candidates. These kagome materials commonly bear key QSL characteristics, such as fractionalized spin excitations and the absence of long-range magnetic order. Notwithstanding, the presence of Zn–Cu antisite mixing hinders the determination of the intrinsic ground state of KHAFs. Rather, this mixing along with lattice imperfections and magnetic disorder leads to the coexistence of gapped singlets and gapless states[36], masking the pristine kagome QSL state. The recently discovered $YCu_3(OD)_{6+x}Br_{3-x}$ (abbreviated as YCu_3) is a promising addition to the kagome QSL system[37–39]. Unlike herbertsmithite, YCu_3 is nearly free from site-disorder-induced orphan spins, whereas the random distribution of OD^-/Br^- introduces exchange randomness. Despite this quenched bond randomness, a kagome lattice of Cu^{2+} is globally undistorted. Singularly, YCu_3 exhibits no magnetic ordering or freezing down to 50 mK and its specific heat displays a nearly quadratic T dependence, reminiscent of a Dirac-like QSL. Considering a moderate exchange interaction of $J \approx 63$ K (see below) and negligible intersite mixing, YCu_3 could serve as a valuable model system for investigating the predicted 1/9 plateau phase.

Here we present a comprehensive study of the zero-field and field-induced phases in YCu_3 by employing various thermodynamic and Raman spectroscopic techniques. Our specific heat, thermal conductivity and Raman scattering data evince the presence of fractionalized spinon excitations. The most salient finding is the observation of the highly sought-after 1/9 plateau phase at a critical magnetic field of $\mu_0 H_{1/9} = 15$–21 T, making it accessible for further experimental exploration.

Results

Specific heat and thermal conductivity

To gain insights into the ground state and low-lying excitations, we first turn to the specific heat and thermal conductivity of YCu_3. Figure 1a presents the T dependence of the magnetic specific heat $C_m(T)$, obtained by subtracting a phonon contribution from the total specific heat (Supplementary Fig. 1). Our $C_m(T)$ data match closely with numerical calculations for a KHAF[39] (pink line and green triangles), capturing the high-T broad maximum at $T_{max} \approx 0.67J$. From the maximum temperature $T_{max} = 42$ K, we estimate the exchange interaction as $J \approx 63$ K. On heating towards $T \approx 4J$, the magnetic entropy $S_m(T)$, calculated by integrating C_m/T, approaches the expected value R ln 2 for an $s = 1/2$ system (dashed line in Fig. 1b), where R is the gas constant. Compared to the theoretical curves, the low-T behaviour of C_m reveals two anomalies: a suppressed hump at $T \approx 0.1J$ and a weak peak at $T^* \approx 2$ K that are ascribed to bond randomness and the Dzyaloshinskii–Moriya (DM) interaction born from bond randomness[40], respectively. However, only a small amount of entropy (3% of R ln 2) is released below the $T^* \approx 2$ K anomaly, indicative of the freezing of a small fraction of local magnetic moments. By resorting to the $T^*/D_c \approx 0.91$ relation[40] between the T^* anomaly in the specific heat and the out-of-plane DM anisotropy D_c, we further determine $D_c \approx 2.2$ K ($=0.035J$), which is significantly smaller than the critical value of $D_{crit} \approx 0.1J$ that separates a QSL from a magnetically ordered phase[41]. We stress that unlike other Cu-based kagome compounds, the out-of-plane DM anisotropy in YCu_3 is not strong enough to disrupt the QSL phase. At the very low temperatures of $T = 0.3$–1 K, we observe a quadratic T dependence $C_m \propto T^2$. Below 0.3 K, deviations from the T^2 behaviour are ascribed to the nuclear Schottky contribution or the destabilization of the QSL against random singlets[42].

The thermal conductivity κ_{xx} conveys valuable information about the presence or absence of itinerant low-energy excitations. Figure 1d plots $\kappa(T)$ versus T on a log–log scale. Notably, $\kappa_{xx}(T)$ shows a gradual increase with increasing T across the whole measured temperature range. This behaviour suggests that phonons alone are insufficient to account for the heat transport. Furthermore, the semi-log plot of κ_{xx}/T versus T (Fig. 1e) reveals distinct humps and a dip in the κ versus T data. The dip of $\kappa_{xx}(T)$ alludes to the suppression of fractionalized excitations, possibly due to enhanced phonon–spinon scattering. To inspect whether the low-T κ_{xx} data contain signatures of itinerant spinons,

https://doi.org/10.1038/s41567-023-02318-7

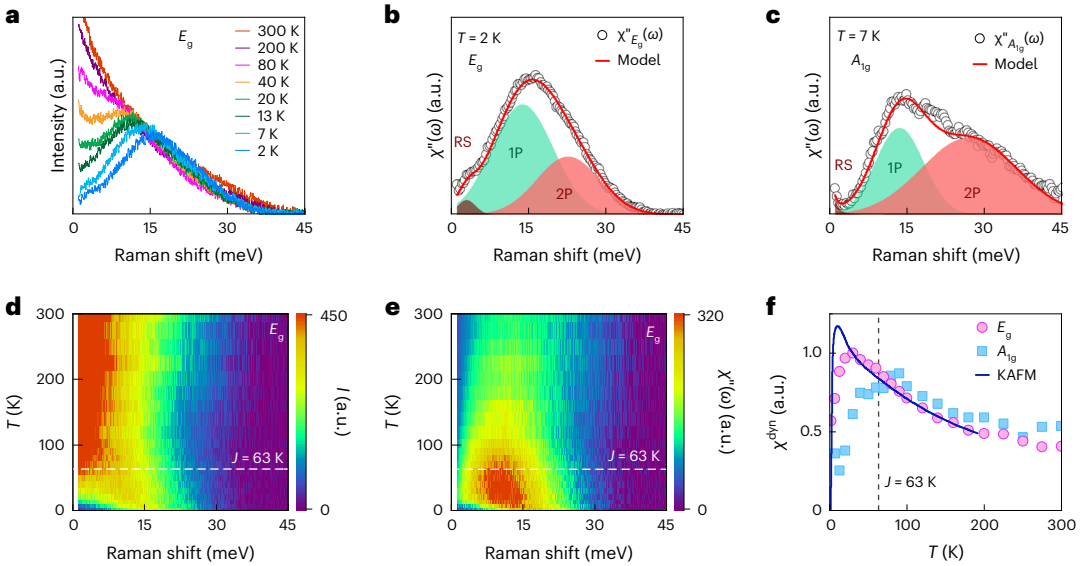

Fig. 2 | Spinon continuum and dynamic Raman susceptibility of $YCu_3(OD)_{6.5}Br_{2.5}$. **a**, Temperature dependence of the magnetic Raman spectra obtained after subtracting phonon peaks in the E_g channel. **b**,**c**, Representative Raman susceptibility $\chi''(\omega)$ (open circles) in the E_g channel at $T = 2$ K (**b**) and in the A_{1g} channel at $T = 7$ K (**c**). The magnetic excitation is decomposed into three components: 1P (turquoise shading) and 2P (salmon) spinon–antispinon excitations with an additional low-energy excitation (RS; brown). The red solid lines represent the sum of three Gaussian line profiles. **d**,**e**, Colour plots of the Raman intensity $I_{E_g}(\omega)$ (**d**) and $\chi''_{E_g}(\omega, T)$ (**e**) in the T–ω plane. The horizontal dashed lines indicate the temperature scale of the antiferromagnetic exchange strength $J = 63$ K determined from the specific heat. **f**, Temperature dependence of the dynamic Raman susceptibilities $\chi^{dyn}_{E_g}(T)$ (pink circles) and $\chi^{dyn}_{A_{1g}}(T)$ (cyan squares) deduced from $\chi''(\omega)$s through the Kramers–Kronig relation plotted together with the theoretical static magnetic susceptibility (KAFM, blue solid line) for a perfect kagome lattice. a.u., arbitrary units.

we analyse the κ_{xx}/T versus T plot in Fig. 1f by fitting it to $\kappa/T = \kappa_0 + aT$. We identify a quadratic T dependence below 0.6 K and a negligibly small κ_0, consistent with recent thermal conductivity measurements[43]. The latter suggests that itinerant fermionic contributions are largely quenched due to the bond randomness. Overall, our κ_{xx} data signify the impact of phonon–spinon interactions and bond randomness on the heat conduction of the YCu_3 system.

Spinon–antispinon pair excitations

To elucidate the characteristics and dynamics of fractional spinon excitations, we conducted Raman scattering experiments with the (XX) and (XY) polarization configurations, corresponding to the $A_{1g} + E_g$ and E_g symmetry channels, respectively. In Fig. 2 and Supplementary Figs. 2–6, we present the temperature and polarization dependencies of Raman spectra. These have sharp phonon peaks superimposed onto a broad magnetic continuum. Hereafter, we focus solely on the magnetic excitations obtained after subtracting the phonon peaks from the as-measured spectra. Further, we calculate the magnetic Raman susceptibility $\chi''(\omega)$ by correcting the Bose factor $n(\omega) = 1/[1\exp(\hbar\omega/k_BT) - 1]$ using the relation $I(\omega) = (1 + n(\omega))\chi''(\omega)$. As plotted in Fig. 2a, the magnetic continuum centred around 15 meV at low temperatures experiences a gradual softening and damping with increasing T.

To a first approximation, the magnetic Raman spectral weight is dominated by spin-number-conserving scattering processes ($\Delta S = 0$). For a KHAF, these processes involve one-pair (1P) and two-pair (2P) spinon–antispinon excitations[44]. To differentiate each contribution, we decomposed the magnetic $\chi''(\omega)$ into three Gaussian profiles, denoted by the colour shadings (P1, P2 and RS (random singlet)) in Fig. 2b,c. We discuss other models in Supplementary Figs. 4 and 5. The 1P excitation is centred at 13 meV (~4.6χJ) and the 2P component has a maximum at $T^{exp}_{2p} = 22$ meV (~7.8χJ) and extends up to $T^{exp}_{2c} = 36$ meV (~12.8χJ) with the adjustable parameter $\chi = 0.5$ (~$2\chi_s$). Here we note that the χ parameter is linked to the renormalization parameter $\chi_s = 0.221$ of the spinon bandwidth[6,39]. In particular, the observed peak energy and spectral width of the 2P excitation are in accordance with the theoretical values of $T^{th}_{2p} = (7–8)\chi J$ and $T^{th}_{2c} = 12\chi J$, which are computed for a kagome QSL state. These experimental observations are consistent with the spectra reported in several spin-1/2 kagome systems, including herbertsmithite and Zn-barlowite[44–47].

In contrast to YCu_3, its magnetic counterpart $YCu_3(OH)_6Cl_3$ exhibits a sharp excitation in the magnetically ordered state below $T_N = 15$ K (ref. 48), which corresponds to one-magnon scattering born out of the 1P excitation (Supplementary Fig. 5). The lack of magnon excitations validates the spinon assignment. Apart from the prominent spinon excitations, we are able to identify another magnetic contribution (RS) at frequencies below 5–6 meV, which is attributed to bond-randomness-induced random singlets. Besides, a comparison of $\chi''_{E_g}(\omega, T)$ and $\chi''_{A_{1g}}(\omega, T)$, as shown in Fig. 2b,c, reveals their close resemblance, except for the dominance of the 2P component over the 1P component in the A_{1g} spinon continuum. This trend is in compliance with the theoretical prediction[44]. However, the only partial suppression of the 1P spectral weight in the A_{1g} channel may be due to the random occupation of OD^-/Br^-.

As evident from the colour map of the Raman intensity $I_{E_g}(\omega)$ and $\chi''_{E_g}(\omega, T)$ in Fig. 2d,e, the spinon excitations dissolve into quasielastic scattering at the temperature scale of $J = 63$ K (see the horizontal dashed lines). The 1P and 2P excitations are resolvable for temperatures below J, whereas their peak energies slightly increase as T approaches 0 K (Supplementary Figs. 7–10). By employing the Kramers–Kronig relation, we derive the dynamic Raman susceptibility $\chi^{dyn} = \frac{2}{\pi}\int_0^\infty \frac{\chi''(\omega)}{\omega} d\omega$ from the magnetic Raman response. Figure 2f plots the temperature dependence of $\chi^{dyn}(T)$ evaluated by integrating the Raman conductivity $\chi''(\omega)/T$ up to 45 meV in the A_{1g} and E_g channels. For temperatures above J, $\chi^{dyn}_{E_g}(T)$ and $\chi^{dyn}_{A_{1g}}(T)$ scale perfectly with the static susceptibility $\chi^{th}_{dc}(T)$ computed for an ideal kagome antiferromagnet. Compared to $\chi^{th}_{dc}(T)$, however, $\chi^{dyn}_{E_g}(T)$ and $\chi^{dyn}_{A_{1g}}(T)$, defined as the dynamic limit of $\chi^{static} = \lim_{\boldsymbol{k}\to 0}\chi(\boldsymbol{k}, \omega = 0)$, are

https://doi.org/10.1038/s41567-023-02318-7

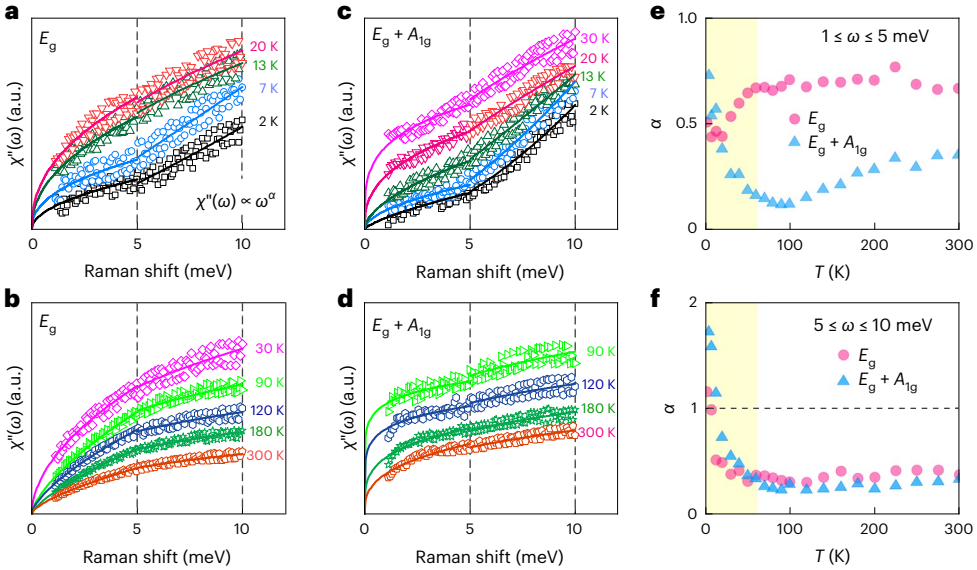

Fig. 3 | Power-law analysis of magnetic Raman susceptibility. a–d, Low-frequency Raman susceptibilities at selected temperatures in the E_g channel for $T = 2$–20 K (**a**) and $T = 30$–300 K (**b**) and in the $E_g + A_{1g}$ channel for $T = 2$–30 K (**c**) and $T = 90$–300 K (**d**). The vertical dashed lines mark two energy regimes: 1–5 and 5–10 meV. The solid lines are power-law fittings to $\chi''(\omega) \propto \omega^{\alpha}$. **e**,**f**, Temperature dependence of the extracted exponent α in the E_g and $E_g + A_{1g}$ channels and the two different energy windows: 1–5 meV (**e**) and 5–10 meV (**f**). The horizontal dashed line denotes $\alpha = 1$.

systematically reduced for temperatures below $J/2$ and J, respectively. This behaviour is largely consistent with the repression of spinon excitation observed in the A_{1g} channel[44] (Fig. 2b,c).

Power-law dependence of spinon Raman susceptibility

Next, we examine the low-energy Raman susceptibility. We attempted to fit the magnetic Raman susceptibility to a power law $\chi''(\omega) \propto \omega^{\alpha}$ in the energy range below 10 meV, in which the contribution from 2P spinon excitations is negligible. As shown in Fig. 3a–d, we could identify two distinct power-law behaviours in two energy intervals for both scattering channels: (1) $\omega = 1$–5 meV and (2) $\omega = 5$–10 meV. The piece-wise power-law behaviour stems from the random-singlet-like excitations present up to 5–6 meV (RS in Fig. 2b). The extracted exponents are plotted as a function of temperature in Fig. 3e,f. In the $\omega = 1$–5 meV regime, on cooling through $J = 63$ K (yellow shading), the exponent drops from $\alpha = 0.7$ to 0.5 for the E_g channel, whereas it increases from $\alpha = 0.15$ to 0.72 for the $A_{1g} + E_g$ channel. We recall that the sublinear behaviour is a hallmark of random singlets[42], which create an abundant low-energy density of states (DOS) of the form $\rho(\omega) \approx \omega^{-\gamma}$. Thus, we conclude that the presence of bond randomness modifies the spectral form of the low-energy DOS, as hinted at by the thermodynamic quantities discussed previously. In the $\omega = 5$–10 meV interval, on approaching zero kelvin, the exponents increase to $\alpha = 1.15$ and 1.72 for the E_g and $A_{1g} + E_g$ channels, respectively. This switch from a sublinear ($\alpha < 1$) to a superlinear behaviour ($\alpha > 1$) in the magnetic $\chi''(\omega)$ suggests that the spinon excitations inherent to KHAFs prevail at higher energies, at which perturbative effects become insignificant.

One-ninth magnetization plateau

Finally, we address the possibility that YCu_3 hosts a desired 1/9 magnetization plateau state. The $s = 1/2$ kagome model predicts a series of magnetization plateaus at $m = 1/9$, 1/3, 5/9 and 7/9. Among these plateaus, the 1/3, 5/9 and 7/9 plateaus can be envisioned as zero, one and two hexagonal magnons, while the edge spins of the hexagram are fully polarized[21–24]. By contrast, the 1/9 plateau is rooted in a different origin involving entangled spins.

Figure 4a presents the high-field magnetization curve $m = M/M_S$ plotted against $\mu_0 H/J_m$ ($J_m = 45$ K; see below) at $T = 2$ K for the field orientation $H \parallel ab$. The pulsed-field $M(H)$ (magenta circles) is scaled to the low-field data from a superconducting quantum interference device (SQUID; yellow triangles) and normalized by the saturation magnetization $M_S = gS\mu_B$ (g is the g factor). As the applied field increases up to 60 T, YCu_3 exhibits two consecutive magnetic phases, inferred from two steplike increases of $m(H)$ at $\mu_0 H_{1/9} \approx 18$–23 T and $\mu_0 H_{1/3} \sim 50$ T. The dips in the field derivative dm/dH (grey squares) confirm the presence of magnetization plateaus. To identify their origin, we compare the experimental $m(H)$ to the calculated magnetization process (blue line) for the spin-1/2 KHAF[26]. The lower-field magnetization plateau is associated with the predicted 1/9 plateau.

To investigate the stability of the 1/9 magnetization plateau, we further measured the in-plane and out-of-plane magnetization up to 25 T at $T = 0.5$ K. Our ^{3}He magnetization data, presented in Fig. 4b, substantiate a robust $m = 1/9$ plateau when the magnetic field is applied perpendicular to the kagome plane ($H \parallel c$; azure squares). The lower and upper critical fields correspond to $\mu_0 H^c_{c1} = 15.4$ T and $\mu_0 H^c_{c2} = 18.3$ T, respectively (vertical arrows in the violet line). For the in-plane $m(H)$, the expected 1/9 plateau exhibits a finite slope, whereas the critical fields shift to higher fields $\mu_0 H^{ab}_{c1} = 16.8$ T and $\mu_0 H^{ab}_{c2} = 21.1$ T (vertical arrows in the coral line). The observed anisotropic behaviour of $m(H)$ with respect to the field orientation is attributed to the g-factor anisotropy, DM anisotropy and in-plane longer-range interactions. The magnitude of the out-of-plane DM component amounts to $D_c \approx 2.2$ K, which is found to be comparable to the width of the out-of-plane $m = 1/9$ plateau ($\Delta\mu_0 H_{1/9} \approx 2.9$ T). The robustness of the out-of-plane $m = 1/9$ plateau suggests that perturbative terms, including the D_c component, are not sufficiently strong to destabilize the $m = 1/9$ state. Conversely, the finite slope observed in the in-plane $m(H)$ within the anticipated plateau regime indicates that the in-plane DM component D_{ab} and in-plane longer-range interactions induce a mixing of the $m = 1/9$ ground state with its excited states. For $s = 1/2$ KHAFs, the in-plane DM component D_{ab} enhances the magnetic susceptibility[41]. Indeed, we can observe the low-T upturn of $\chi(T)$ in Supplementary Fig. 1a. However, note that the bond randomness can also contribute to the enhancement of $\chi(T)$ at low temperatures due to the rich low-energy DOS. Thus, further investigation is needed to accurately determine the strength of the D_{ab} component

https://doi.org/10.1038/s41567-023-02318-7

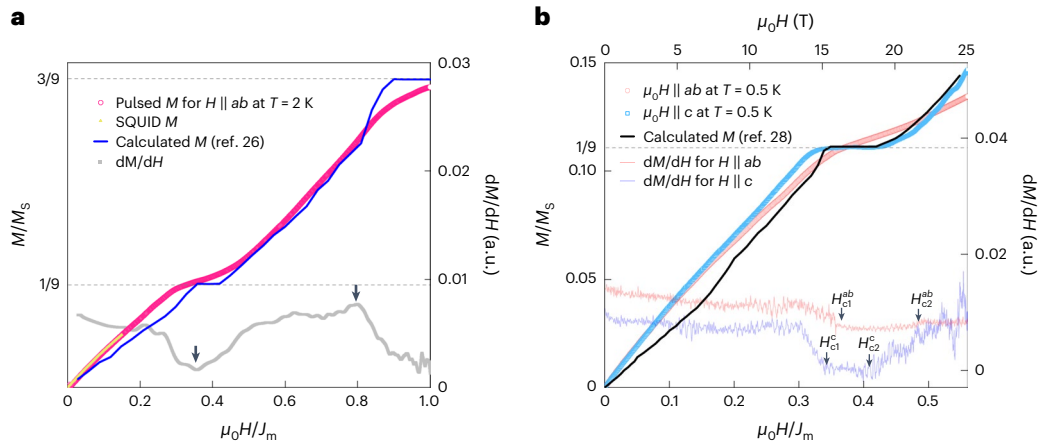

Fig. 4 | High-field magnetization and 1/9 magnetization plateau. a, The pulsed-field magnetization $m(H)$ of YCu_3 (magenta circles) and its field derivative dm/dH (grey squares) measured at $T = 2$ K with a non-destructive pulse magnet up to 60 T. The blue solid line represents the calculated magnetization for the spin-1/2 KHAF, taken from ref. 26. The pulsed-field data are calibrated to the low-field SQUID data (yellow triangles). **b**, Comparison of the in-plane (orange circles) and out-of-plane (azure squares) magnetization measured at $T = 0.5$ K, along with the calculated curve[28] (solid line). The vertical arrows in the dm/dH data (violet and coral lines) indicate the lower and upper critical fields of the 1/9 magnetization plateau. The horizontal dashed lines denote the theoretical 1/9 and 3/9 magnetization plateaus.

and to elucidate whether its putative large value ($D_{ab} > D_c \approx 2.2$ K) is primarily responsible for the instability of the $m = 1/9$ phase.

Finally, by comparing the theoretical predictions with the out-of-plane $m(H,T = 0.5\ \text{K})$, the effective exchange interaction J_m is evaluated as $J_m = 45$ K, which is smaller than the $J \approx 63$ K estimated by the specific heat measurements. This difference between J_m and J is attributed to the influence of a distribution of exchange interactions $[J - \Delta J, J + \Delta J]$. The magnitude of this exchange randomness can be estimated as $\Delta J = |J - J_m| \approx 18$ K, considering that J is deduced from the centroid of C_m, whereas J_m is determined by the onset of the $m = 1/9$ magnetization plateau.

Discussion and conclusion

Based on our experimental data, it is evident that YCu_3 occupies a unique parameter range among kagome antiferromagnets. Despite the presence of small DM anisotropies and moderate bond randomness, the predicted 1/9 magnetization plateau remains robust and immune to perturbative interactions when a magnetic field is applied perpendicular to the kagome plane. This may be because the out-of-plane DM component ($D_c \ll 0.1J$) alone is not strong enough to destroy a QSL ground state. On the other hand, the in-plane perturbative terms, including the in-plane D_{ab} component and longer-range interactions, could be stronger than the out-of-plane terms, thereby leading to the destabilization of the $m = 1/9$ plateau. Although the field-induced phase exhibits some resilience against perturbations, the unavoidable perturbative interactions seem to modify the intrinsic kagome QSL. Given the significance of distinguishing between different QSL scenarios in the kagome lattice, we delve into the ramifications of our thermodynamic and spectroscopic data in relation to a Z_2 gapped versus a gapless U(1) liquid state. The dynamical crossover and typical persistence in an incipient QSL provide a conceptual framework for the following discussion[49].

A key characteristic of QSLs is the emergence of fractionalized excitations, as demonstrated by our Raman scattering data (Figs. 2 and 3). Note that the Raman spectrum and its associated susceptibility were specifically computed for the U(1) Dirac QSL, which provides a starting point for a detailed comparison. In an ideal KHAF, the low-ω magnetic Raman spectrum follows a ω^3 dependence, as long as the matrix element vanishes for all 1P spinon–antispinon excitations[44]. However, when perturbative interactions introduce a finite matrix element, then $\chi''(\omega)$ emulates the DOS of low-energy excitations, often leading to a weaker ω^α dependence ($1 < \alpha < 3$). Since Dirac spinons possess a linear dispersion, $\alpha = 1$ occupies a special point. In this context, the superlinear power-law behaviour ($\alpha = 1.15$ for the E_g scattering channel and 1.72 for the $A_{1g} + E_g$ channel) observed in the energy range $\omega = 5$–10 meV suggests that the high-energy spinons retain a Dirac-like nodal structure. Below 5 meV, however, the YCu_3 system is substantially affected by perturbations, and the typical persistence of Dirac spinons is no longer valid. Consequently, the lower-energy fractional excitations experience some modifications from the Dirac dispersion. This deviation is reflected in the sublinear power-law behaviour observed in the Raman spectra below 5 meV.

Next, we turn to the thermodynamic and nuclear magnetic resonance (NMR) signatures of QSLs. For a Dirac QSL, both the specific heat and the NMR spin-lattice relaxation rate $1/T_1$ are expected to exhibit a T^2 dependence[6]. Indeed, we observe a $C_m \propto T^2$ behaviour over a limited temperature range of $T = 0.3$–1 K. However, the NMR spin-lattice relaxation rate $1/T_1$ shows a $T^{0.5}$ dependence below 3 K and a $T^{0.8}$ dependence in the temperature range $T = 3.5$–14 K (Supplementary Fig. 11), which deviates from the expected T^2 behaviour. Furthermore, the absence of a notable linear T term in the thermal conductivity implies that the formation of a spinon Fermi surface is highly unlikely. Taken together, it seems that the YCu_3 system loses the characteristic features of the Dirac spinons in the low-energy and low-temperature regime.

To conclude, we have observed the $m = 1/9$ magnetization plateau in the kagome antiferromagnet YCu_3. The underlying kagome physics appears to dictate the spin dynamics and field-induced phases of YCu_3, possibly due to the limited impact of perturbative terms. The critical field required to access the $m = 1/9$ plateau is readily reached by superconducting magnets, rendering YCu_3 an unparalleled platform for studying field-induced quantum entangled phases. This discovery lays the groundwork for deeper exploration and theoretical modelling that may provide a comprehensive understanding of the exotic 1/9 plateau state.

Online content

Any methods, additional references, Nature Portfolio reporting summaries, source data, extended data, supplementary information, acknowledgements, peer review information; details of author contributions and competing interests; and statements of data and code availability are available at https://doi.org/10.1038/s41567-023-02318-7.

References

1. Balents, L. Spin liquids in frustrated magnets. *Nature* **464**, 199–208 (2010).
2. Savary, L. & Balents, L. Quantum spin liquids: a review. *Rep. Prog. Phys.* **80**, 016502 (2017).
3. Zhou, Y., Kanoda, K. & Ng, T.-K. Quantum spin liquid states. *Rev. Mod. Phys.* **89**, 025003 (2017).
4. Broholm, C. et al. Quantum spin liquids. *Science* **367**, eaay0668 (2020).
5. Waldtmann, C. et al. First excitations of the spin 1/2 Heisenberg antiferromagnet on the kagomé lattice. *Eur. Phys. J. B* **2**, 501–507 (1998).
6. Ran, Y., Hermele, M., Lee, P. A. & Wen, X. G. Projected-wave-function study of the spin-1/2 Heisenberg model on the kagomé lattice. *Phys. Rev. Lett.* **98**, 117205 (2007).
7. Iqbal, Y., Becca, F. & Poilblanc, D. Valence-bond crystal in the extended kagome spin-1/2 quantum Heisenberg antiferromagnet: a variational Monte Carlo approach. *Phys. Rev. B* **83**, 100404(R) (2011).
8. He, Y. C., Zaletel, M. P., Oshikawa, M. & Pollmann, F. Signatures of Dirac cones in a DMRG study of the kagome Heisenberg model. *Phys. Rev. X* **7**, 031020 (2017).
9. Liao, H. J. et al. Gapless spin-liquid ground state in the S=1/2 kagome antiferromagnet. *Phys. Rev. Lett.* **118**, 137202 (2017).
10. Yan, S., Huse, D. A. & White, S. R. Spin-liquid ground state of the S=1/2 kagome Heisenberg antiferromagnet. *Science* **332**, 1173 (2011).
11. Jiang, H. C., Wang, Z. & Balents, L. Identifying topological order by entanglement entropy. *Nat. Phys.* **8**, 902–905 (2012).
12. Depenbrock, S., McCulloch, I. P. & Schollwöck, U. Nature of the spin-liquid ground state of the S=1/2 Heisenberg model on the kagome lattice. *Phys. Rev. Lett.* **109**, 067201 (2012).
13. Kolley, F., Depenbrock, S., McCulloch, I. P., Schollwöck, U. & Alba, V. Phase diagram of the J_1–J_2 Heisenberg model on the kagome lattice. *Phys. Rev. B* **91**, 104418 (2015).
14. Mei, J. W., Chen, J. Y., He, H. & Wen, X. G. Gapped spin liquid with Z_2 topological order for the kagome Heisenberg model. *Phys. Rev. B* **95**, 235107 (2017).
15. Hida, K. Magnetization process of the S=1 and 1/2 uniform and distorted kagome Heisenberg antiferromagnets. *J. Phys. Soc. Jpn* **70**, 3673 (2001).
16. Zhitomirsky, M. E. Field-induced transitions in a kagome antiferromagnet. *Phys. Rev. Lett.* **88**, 057204 (2004).
17. Zhitomirsky, M. E. & Tsunetsugu, H. Exact low-temperature behavior of a kagome antiferromagnet at high fields. *Phys. Rev. B* **70**, 100403(R) (2004).
18. Honecker, A., Schulenburg, J. & Richter, J. Magnetization plateaus in frustrated antiferromagnetic quantum spin models. *J. Phys. Condens. Matter* **16**, S749 (2004).
19. Nakano, H. & Sakai, T. Magnetization process of kagome-lattice Heisenberg antiferromagnet. *J. Phys. Soc. Jpn* **79**, 053707 (2010).
20. Sakai, T. & Nakano, H. Critical magnetization behavior of the triangular- and Kagome-lattice quantum antiferromagnets. *Phys. Rev. B* **83**, 100405(R) (2011).
21. Nishimoto, S., Shibta, N. & Hotta, C. Controlling frustrated liquids and solids with an applied field in a kagome Heisenberg antiferromagnet. *Nat. Commun.* **4**, 2287 (2013).
22. Capponi, S. et al. Numerical study of magnetization plateaus in the spin-1/2 kagome Heisenberg antiferromagnet. *Phys. Rev. B* **88**, 144416 (2013).
23. Huerga, D., Capponi, S., Dukelsky, J. & Ortiz, G. Staircase of crystal phases of hard-core bosons on the Kagome lattice. *Phys. Rev. B* **94**, 165124 (2016).
24. Plat, X., Momoi, T. & Hott, C. Kinetic frustration induced supersolid in the S=1/2 kagome lattice antiferromagnet in a magnetic field. *Phys. Rev. B* **98**, 014415 (2018).
25. Schnack, J., Schulenburg, J. & Richter, J. Magnetism of the N=42 kagome lattice antiferromagnet. *Phys. Rev. B* **98**, 094423 (2018).
26. Picot, T., Ziegler, M., Orus, R. & Poilblanc, D. Spin-S kagome quantum antiferromagnets in a field with tensor networks. *Phys. Rev. B* **93**, 060407 (2016).
27. Okuma, R. et al. A series of magnon crystals appearing under ultrahigh magnetic fields in a kagomé antiferromagnet. *Nat. Commun.* **10**, 1229 (2019).
28. Fang, D.-Z, Xi, N., Ran, S.-J. & Su, G. Nature of the 1/9-magnetization plateau in the spin-1/2 kagome Heisenberg antiferromagnet. *Phys. Rev. B* **107**, L220401 (2023).
29. Shores, M. P., Nytko, E. A., Bartlett, B. M. & Nocera, D. G. A structurally perfect S=1/2 kagomé antiferromagnet. *J. Am. Chem. Soc.* **127**, 13462 (2005).
30. Mendels, P. & Bert, F. Quantum kagome antiferromagnet $ZnCu_3(OH)_6Cl_2$. *J. Phys. Soc. Jpn* **79**, 011001 (2010).
31. Han, T.-H. et al. Fractionalized excitations in the spin-liquid state of a kagome-lattice antiferromagnet. *Nature* **492**, 406–410 (2012).
32. Norman, M. R. Colloquium: herbertsmithite and the search for the quantum spin liquid. *Rev. Mod. Phys.* **88**, 041002 (2016).
33. Fak, B. et al. Kapellasite: a kagome quantum spin liquid with competing interactions. *Phys. Rev. Lett.* **109**, 037208 (2012).
34. Tustain, K. et al. From magnetic order to quantum disorder in the Zn-barlowite series of S=1/2 kagomé antiferromagnets. *NPJ Quantum Mater.* **5**, 74 (2020).
35. Feng, Z. et al. Gapped spin-1/2 spinon excitations in a new kagome quantum spin liquid compound $Cu_3Zn(OH)_6FBr$. *Chin. Phys. Lett.* **34**, 077502 (2017).
36. Wang, J. et al. Emergence of spin singlets with inhomogeneous gaps in the kagome lattice Heisenberg antiferromagnets Zn-barlowite and herbertsmithite. *Nat. Phys.* **17**, 1109 (2021).
37. Chen, X.-H. et al. Quantum spin liquid candidate $YCu_3(OH)_6Br_2[Br_x(OH)_{1-x}]$ (x=0.5): with an almost perfect kagome layer. *J. Magn. Magn. Mater.* **512**, 167066 (2020).
38. Zeng, Z. et al. Possible Dirac quantum spin liquid in a kagome quantum antiferromagnet $YCu_3(OH)_6Br_2[Br_x(OH)_{1-x}]$. *Phys. Rev. B* **105**, L121109 (2022).
39. Liu, J. et al. Gapless spin liquid behavior in a kagome Heisenberg antiferromagnet with randomly distributed hexagons of alternate bonds. *Phys. Rev. B* **105**, 024418 (2022).
40. Arh, T. et al. Origin of magnetic ordering in a structurally perfect quantum kagome antiferromagnet. *Phys. Rev. Lett.* **125**, 027203 (2020).
41. Hering, M. & Reuther, J. Functional renormalization group analysis of Dzyaloshinksy–Moriya and Heisenberg spin interactions on the kagome lattice. *Phys. Rev. B* **95**, 054418 (2017).
42. Kawamura, H. & Uematsu, K. Nature of the randomness-induced quantum spin liquids in two dimensions. *J. Phys. Condens. Matter* **31**, 504003 (2019).
43. Hong, X. et al. Heat transport of the kagomé Heisenberg quantum spin liquid candidate $YCu_3(OH)_{6.5}Br_{2.5}$: localized magnetic excitations and spin gap. *Phys. Rev. B* **106**, L220406 (2022).
44. Ko, W.-H. et al. Raman signature of the U(1) Dirac spin-liquid state in the spin-$\frac{1}{2}$ kagome system. *Phys. Rev. B* **81**, 024414 (2010).
45. Wulferding, D. et al. Interplay of thermal and quantum spin fluctuations in the kagome lattice compound herbertsmithite. *Phys. Rev. B* **82**, 144412 (2010).

46. Wulferding, D., Choi, Y. S., Lee, W. J. & Choi, K.-Y. Raman spectroscopic diagnostic of quantum spin liquids. *J. Phys. Condens. Matter* **32**, 043001 (2020).
47. Fu, Y. et al. Dynamical fingerprint of fractionalized excitations in single-crystalline $Cu_3Zn(OH)_6FBr$. *Nat. Commun.* **12**, 3048 (2021).
48. Zorko, A. et al. Coexistence of magnetic order and persistent spin dynamics in a quantum kagome antiferromagnet with no intersite mixing. *Phys. Rev. B* **99**, 214441 (2019).
49. Rousochatzakis, I., Kourtis, S., Knolle, J., Moessner, R. & Perkins, N. B. Quantum spin liquid at finite temperature: proximate dynamics and persistent typicality. *Phys. Rev. B* **100**, 045117 (2019).

Methods

Crystal growth and magnetic characterization

Single crystals of $YCu_3(OH)_{6.5}Br_{2.5}$ and deuterated $YCu_3(OD)_{6.5}Br_{2.5}$ were synthesized by a hydrothermal method. $Cu(NO_3)_2{\cdot}3H_2O$ (10.0 mmol), $Y(NO_3)_3{\cdot}6H_2O$ (20.0 mmol) and KBr (60.0 mmol) were mixed in 8.0 ml of distilled water or D_2O (7.0 ml). Each of those mixtures was transferred into a 100 ml Teflon-lined stainless-steel autoclave, heated up to 300 K at a rate of 1 K min^{-1} and then maintained for 3 hr. The autoclave was then cooled down to room temperature at a rate of 0.1 K min^{-1}. Green hexagonal tablet crystals were isolated by washing with distilled water.

We measured the d.c. magnetization ($\mu_0 H = 0$–7 T) and magnetic susceptibility ($T = 2$–350 K in an applied magnetic field of $\mu_0 H = 1$ T) using a SQUID vibrating sample magnetometer (VSM; Quantum Design), as presented in Supplementary Note 1.

Specific heat and thermal conductivity

The thermal conductivity was measured by the four-probe steady-state method using Leiden CF-150 dilution refrigerator and Quantum Design physical property measurement system (PPMS). Temperature differences were measured using two RuO_x sensors (Rx102A) in the dilution refrigerator or two sensors (Cx-1010, Cernox) in the PPMS. Four 50 μm silver wires were used to make a good thermal link between the sample and thermometers. A heat current was applied parallel to the *ab* plane of the sample. All data were measured within a temperature difference of dT, satisfying $dT/T_0 < 1.5\%$, where T_0 is the base temperature of the specimen.

High-field magnetization

Pulsed-field magnetization was measured on high-quality single-crystalline samples using the National High Magnetic Field Laboratory's pulsed-field magnetometry up to 60 T and at the Institute for Materials Research, Tohoku University, using a multilayer pulse magnet up to 30 T. The pickup coil was a radially compensated coil wound from 50 American gauge copper wire. The samples were inserted into a nonmagnetic ampule and fixed with vacuum grease. The voltage signal induced in the coil in the pulsed fields was proportional to the derivative of the magnetization with time. The voltage was numerically integrated and calibrated with the magnetization obtained in d.c. magnetization measured using the SQUID-VSM (Quantum Design). For each field-dependent magnetization curve, two data points, one with the sample in and one with it out of the coil signals, were collected under identical conditions, and the sample-out signal was subtracted from the sample-in signal to remove background signals.

Raman scattering measurements

Raman scattering measurements were carried out in exact backscattering geometry using the excitation line $\lambda = 561$ nm laser (Oxxius LCX). We collected the scattered spectra with a TriVista spectrometer (Princeton Instruments, SP-2500i) equipped with a liquid-nitrogen cooled CCD (PyLoN eXcellon). We used a volume Bragg grating notch filter (Optigrate), which enabled low-frequency Raman measurements down to ~10 cm^{-1}. The incident laser was focused on a spot diameter of about 4 μm on the sample surface with a ×40 microscope objective. The laser power was kept below $P = 0.2$ mW to minimize heating effects. The samples were mounted on a liquid helium flow cryostat, while the temperature was varied between $T = 2$ and 300 K.

Data availability

All relevant data supporting the findings of this study are available from the corresponding authors on reasonable request. Source data are provided with this paper.

Acknowledgements

The work at Sungkyunkwan University was supported by the National Research Foundation (NRF) of Korea (grant nos. RS-2023-00209121 and 2020R1A5A1016518). This research was supported by the SungKyunKwan University and the BK21 FOUR (Graduate School Innovation) funded by the Ministry of Education (MOE, Korea) and the National Research Foundation of Korea (NRF). The work at Seoul National University was financially supported by the NRF of Korea funded by the Korean government (grant no. 2019R1A2C2090648), as well as from the Ministry of Education (grant no. 2021R1A6C101B418). A portion of this work was performed at the National High Magnetic Field Laboratory, which is supported by the National Science Foundation (cooperative agreement no. DMR-1644779), the State of Florida and the US Department of Energy. M.L. is supported by the US Department of Energy, Office of Science and National Quantum Information Science Research Centers. D.W. acknowledges support from the Institute of Basic Science (IBS-R009-Y3). S.L. and S.C. acknowledge support from the Institute of Basic Science (IBS-R011-Y3). The work at the Korea Research Institute of the Max Planck Institute and Pohang University of Science and Technology was supported through the NRF funded by the Ministry of Science, ICT and Future Planning of Korea (grant no. 2022M3H4A1A04074153). A portion of the research was performed in the GIMRT program at IMR, Tohoku University. Additionally, M.L. expresses gratitude to G. Timothy Noe II for making a single-wall fridge for use in this experiment.

Author contributions

The experimental project was conceived by K.-Y.C. and S.M.J., who synthesized the single crystals and conducted the magnetic susceptibility measurements. D.W., Y.S.C., S.Y.L. and K.-Y.C. performed the Raman scattering experiments and analysed the Raman data. K.W.N. and K.H.K. measured the thermal conductivity and analysed the thermal conductivity data. M.L. and H.N. carried out the pulsed-field magnetization experiments. T.-H.J., J.-H.P., S.H.L. and S.K.C. measured the specific heat and analysed the specific heat data. C.H.L. performed the NMR experiments. The manuscript was written through the contributions of all authors.

Competing interests

The authors declare no competing interests.

Additional information

Supplementary information The online version contains supplementary material available at https://doi.org/10.1038/s41567-023-02318-7.

Correspondence and requests for materials should be addressed to Kwang-Yong Choi.

Peer review information *Nature Physics* thanks Thuc Mai and the other, anonymous, reviewer(s) for their contribution to the peer review of this work.